Solution Processing Route to Multifunctional Titania Thin Films: Highly Conductive and Photcatalytically Active Nb:TiO_2

Davinder S. Bhachu, Sanjayan Sathasivam, Gopinathan Sankar, David O. Scanlon, Giannantonio Cibin, Claire J. Carmalt, Ivan P. Parkin,* Graeme W. Watson, Salem M. Bawaked, Abdullah Y. Obaid, Shaeel Al-Thabaiti, and Sulaiman N. Basahel*

This paper reports the synthesis of highly conductive niobium doped titanium dioxide (Nb:TiO_2) films from the decomposition of $Ti(OEt)_4$ with dopant quantities of $Nb(OEt)_5$ by aerosol-assisted chemical vapor deposition (AACVD). Doping Nb into the Ti sites results in *n*-type conductivity, as determined by Hall effect measurements. The doped films display significantly improved electrical properties compared to pristine TiO_2 films. For 5 at.% Nb in the films, the charge carrier concentration was 2×10^{21} cm^{-3} with a mobility of 2 cm^2 V^{-1} s^{-1} . The corresponding sheet resistance is as low as 6.5 Ω sq^{-1} making the films suitable candidates for transparent conducting oxide (TCO) materials. This is, to the best of our knowledge, the lowest reported sheet resistance for Nb:TiO_2 films synthesized by vapour deposition. The doped films are also blue in colour, with the intensity dependent on the Nb concentration in the films. A combination of synchrotron, laboratory and theoretical techniques confirmed niobium doping into the anatase TiO_2 lattice. Computational methods also confirmed experimental results of both delocalized (Ti^{4+}) and localized polaronic states (Ti^{3+}) states. Additionally, the doped films also functioned as photocatalysts. Thus, Nb:TiO_2 combines four functional properties (photocatalysis, electrical conductivity, optical transparency and blue colouration) within the same layer, making it a promising alternative to conventional TCO materials.

1. Introduction

Transparent conducting oxides (TCOs) are materials that combine optical transparency with electrical conductivity. In order for materials to be transparent they must display an optical bandgap greater than the highest frequency of visible light (3.1 eV).[1,2] The introduction of impurities into the crystal structure results in donor states near the conduction band if the conductivity is *n*-type.[3–5] These materials underpin the photovoltaic (PV) industry by providing transparent electrodes for thin film amorphous silicon solar cells, dye-sensitized solar cells (DSSC) and flat panel displays in polymer light emitting devices.[6–8]

TCO materials are generally limited to simple binary/ternary oxides that can be doped with aliovalent cations/anions to impart an overall positive charge on the framework material. These dopants are compensated for by electrons, which reside in the conduction band of the

Dr. D. S. Bhachu, Dr. S. Sathasivam, Prof. C. J. Carmalt, Prof. I. P. Parkin
Materials Chemistry Centre
Department of Chemistry
University College London
20 Gordon Street, London WC1H 0AJ, UK
Fax: (+44) 20–7396–1056; Fax: (+44) 20–7679–7463
E-mail: d.bhachu@ucl.ac.uk; i.p.parkin@ucl.ac.uk
Dr. S. Sathasivam
Bio Nano Consulting Ltd
338 Euston Road, London, UK
Prof. G. Sankar, Dr. D. O. Scanlon
University College London
Kathleen Lonsdale Materials Chemistry
20 Gordon Street, London WC1H 0AJ, UK
Dr. D. O. Scanlon Dr. G. Cibin
Diamond Light Source Ltd., Diamond House
Harwell Science and Innovation Campus
Didcot, Oxfordshire OX11 0DE, UK
Prof. G. W. Watson
School of Chemistry and CRANN
Trinity College Dublin
Dublin 2, Ireland
Dr. S. M. Bawaked, Prof. A. Y. Obaid,
Prof. S. Al-Thabaiti, Prof. S. N. Basahel
Chemistry Department
King Abdulaziz University
Saudi Arabia

DOI: 10.1002/adfm.201400338

material to maintain charge neutrality, resulting in degenerate conductivity.[9–11] The most common TCO material is based upon doped In_2O_3.[12–14] Other commercial TCO materials are based on the doped oxides of tin and zinc.[3,10,15–17]

Titanium dioxide, TiO_2, is a nonstoichiometric semiconductor that exhibits outstanding photoelectrochemical (PEC) properties as demonstrated by Fujishima and Honda.[18–22] They showed that TiO_2 can be used for the conversion of solar energy to chemical energy, by essentially using TiO_2 as a photoelectrode for water splitting. Nitrogen doping of TiO_2 is fairly common and the role of nitrogen doped titania grown by CVD has been discussed by Sheel et al.[23] As well as the PEC properties of anatase, TiO_2 also finds applications in photoinduced hydrophilicity, utilized for self-cleaning applications (Pilkington-NSG Activ), which allows for greater wetting of a surface as well as the formation of electron/hole pairs for dirt degradation.[19,21,24–28] It is only recently that TiO_2 has been explored for electronic materials such as resistive memories, diluted magnetic semiconductors and transparent conductors.[29,30]

TiO_2 is an amphoteric semiconductor that exhibits *n*-type conductivity. It is well known that the PEC and electrical properties of TiO_2 can be engineered to certain requirements by modification of the defect chemistry.[29,31] The intrinsic *n*-type conductivity of undoped TiO_2 is given below in terms of the donor regimes, i.e., oxygen vacancies and titanium interstitials.[29] These regimes are more thermodynamically favourable in anatase TiO_2 compared to rutile TiO_2, which may account for the larger conductivity observed for anatase than in rutile.

In order to improve the intrinsic conductivity of TiO_2 modifying the defect nature of the system is essential. The main systems that have been explored to improve the intrinsic conductivity of anatase TiO_2 have been Nb and Ta doped anatase TiO_2. Furubayashi et al. reported high conductivity and high optical transparency of Nb:TiO_2 films epitaxially grown by pulsed laser deposition (PLD).[32] The conductivity of these films was reported to be comparable to tin-doped indium oxide (ITO) type films.

The mechanism for Nb doping in anatase titanium dioxide is such that the Nb^{5+} ions occupy Ti^{4+} sites, resulting in charge compensation by electrons in the conduction band of the material. The extra electrons introduced by Nb become transferred to the Ti sites and is easily shown via XPS data indicating Ti(III) structures. For higher doping levels reduced niobium species can also exist as Nb^{4+}.[31,33] However, the incorporation of Nb^{5+} can also lead to the formation of competing point defects (cation vacancy) to maintain charge neutrality, i.e., a titanium vacancy for every four niobium ions doped into the system. For electrical applications it is essential that thermodynamics favours electron donation over point defect formation.[9,29]

High level Nb doping (≈10 at.%) showed an increase in the bandgap energy relative to un-doped anatase from 3.18 eV to ca. 3.35 eV. It was found that Nb doping greater than 5 at.% caused the Fermi energy level to lie in the conduction band as the number of charge carriers increased, thereby moving the measured bandgap to a higher energy; an example of the Burstein–Moss effect.[5,10,21,34–36] The Nb impurity states form a band above the conduction band minimum, contributing electrons to the unoccupied Ti 3d orbitals. This is in contrast to conventional TCOs that possess conduction band minima dominated by cation *s* orbitals. Furubayashi et al. also found that with increased Nb doping in anatase that the transmittance of the red/infrared region decreased systematically which they attributed to free carrier absorption, giving rise to coloured films.[32]

Niobium doped anatase systems, previously reported in the literature, tend to be uniform films formed primarily via either DC magnetron sputtering or pulsed laser deposition. The advantages of CVD over PVD synthesis are clear; CVD films often give superior adhesion, durability and uniformity.[37] Anatase/rutile TiO_2 has been synthesized by AACVD before but the effect of doping with cations has not been explored to date.[38] Kafizas et al. deposited Nb:TiO_2 by combinatorial atmospheric pressure CVD (c-APCVD).[21] The highest Nb concentration in this combinatorial system was found to be ≈2 at.%. The sheet resistance for these films however, was in the kΩ regime. The photocatalytic activity of these films was assessed and it was found that the photocatalytic activity increased (to UVA and white light) with electrical conductivity. Gordon et al. also deposited Nb:TiO_2 via a spray system in which they grew films ≈2 μm thick with sheet resistances ≈25 Ω sq^{-1}. However, the photocatalytic properties of these films were not investigated.[39]

In this paper, we describe the aerosol assisted chemical vapour deposition (AACVD) synthesis of niobium doped anatase films. AACVD is a solution based variant of the conventional CVD process in which dissolved precursors are nebulized and transported to the CVD reactor by a carrier gas and undergo more conventional CVD processes to react and form a film.[14] AACVD is routinely used for the deposition of metal oxide films.[40] Niobium doped anatase films were synthesized by atomizing $Ti(OEt)_4$ with varying dopant amounts of $Nb(OEt)_5$ in toluene and reacted at 500 °C under a flow of nitrogen. The films were then assessed for their structural, opto-electronic properties as well as photocatalytic properties that are seldom reported. It was found that these films were blue in colour, a desirable property for architectural glazing and displayed low, stable sheet resistances significantly better than those previously reported for Nb:TiO_2 synthesized by CVD, making them ideal candidates for PV devices. To our knowledge, this is the first example of a tinted TCO material that demonstrates photocatalysis. In addition, this is also the first example of Nb:TiO_2 that does not require post-deposition annealing in a reducing atmosphere in order to enhance the conductivity. The films were analysed by a combination of synchrotron and laboratory and techniques to determine the bulk and surface properties of the films. Experimental observations were confirmed by a synergistic ab initio study utilising hybrid density functional theory. Our studies showed direct evidence of Nb substituting on a Ti site in the anatase TiO_2 lattice. Surface studies and computational methods showed a combination of Ti^{3+} states (associated with a localized electron polaron) and Ti^{4+} states (associated with delocalized electron states).

2. Experimental Section

2.1. General Procedure

Depositions were carried out under nitrogen (99.99% from BOC). Precursors were placed in a glass bubbler and an aerosol

mist was created using a piezoelectric device. All chemicals were procured from Aldrich and were utilized as bought.

$Ti(OEt)_4$ (2 g, 8.8 mmol) was dissolved in toluene (25 ml) and $Nb(OEt)_5$ was added in dopant amounts (0–20 mol.%). The resulting solution was stirred for 30 minutes and then atomized. The precursor flow was kept at 0.6 l min^{-1}. The glass substrate was SiO_2, precoated (ca. 50 nm thick SiO_2 barrier layer) standard float glass (NSG) 15 cm × 4 cm × 0.3 cm. A top plate was suspended 0.5 cm above the glass substrate to ensure a laminar flow.

The substrate temperature was kept at 500 °C. Deposition time was 45 minutes. After the deposition the bubblers were closed and the substrates were cooled under a flow of nitrogen.

At the end of the deposition the nitrogen flow through the aerosol was diverted and only nitrogen passed over the substrate. The glass substrate was allowed to cool with the graphite block to less than 100 °C before it was removed. Coated substrates were handled and stored in air. The coated glass substrate was cut into ca. 1 cm × 1 cm squares for subsequent analysis.

2.2. Film Analysis

X-ray diffraction (XRD) was used to analyse the samples in a Bruker-Axs D8 (GADDS) diffractometer. This uses a large 2D area detector to collect large sections of Debye-Scherrer cones produced by a polycrystalline sample. This instrument uses a Cu source for X-ray generation with Cu$K\alpha_1$ and Cu$K\alpha_2$ radiation of wavelengths 1.54056 Å and 1.54439 Å respectively, emitted with an intensity ratio of 2:1, a voltage of 40 kV and current of 30 mA. The angular range of the patterns collected was $10° < 2\theta < 66°$. Le Bail models were fitted to the collected data using General Structure Analysis System (GSAS) and EXPGUI suite in order to determine the unit cell parameters.[41,42]

Scanning electron microscopy (SEM) was performed to determine surface morphology and film thickness using a JEOL JSM-6301F field emission SEM at an accelerating voltage of 5 keV.

The Nb:Ti at.% composition was investigated via wavelength dispersive X-ray (WDX) analysis on a JEOL Superprobe JXA-8600. Compositions were calculated relative to niobium and titanium metal standards measured using PET crystals. The average Nb: Ti% over four area scans (200 mm^2) of each position analysed was taken.

X-ray photoelectron spectroscopy (XPS) was performed a Thermo Scientific K-alpha photoelectron spectrometer using monochromatic Al-K_α radiation. Survey scans were collected in the range 0–1100 eV (binding energy) at a pass energy of 160 eV. Higher resolution scans were recorded for the principal peaks of Ti (2p), Nb (3d), O (1s), C (1s) and Si (2p) at a pass energy of 50 eV. Peak positions were calibrated to carbon and plotted using the CasaXPS software.

Nb/Ti K-edge XAS measurements were carried out at beamline (B18) at the UK synchrotron, Diamond, which operates at 3 GeV and 300 mA. The beam line is equipped with Si(111) double crystal monochromator, ion chambers for measuring incident and transmitted beam intensity and a 9 element Ge fluorescence detector for measurement in fluorescence mode. All the measurements were carried out in fluorescence mode and typically 6 scans were averaged to produce the spectra. X-ray absorption spectra were processed using ATHENA software and subsequent analysis of the EXAFS data were performed using EXCURVE.[43,44]

UV/Visible/near IR spectra were taken using a Perkin Elmer Fourier transform Lambda 950 UV/Vis spectrometer over a wavelength range of 300 nm to 2500 nm in transmission mode. The transmission spectra were taken against an air background.

Hall effect measurements were carried out using the van der Pauw method to determine the sheet resistance, free carrier concentration (N) and mobility (μ). A square array of ohmic contacts arranged on 1 cm^2 samples were then subjected to an input current of 1 mA and a calibrated magnetic field of 0.58 T. The transverse voltage was then measured. The measurement was repeated by reversing the direction of the magnetic field and the current.

Prior to the photocatalysis study, the samples were washed with distilled water, rinsed in isopropanol and irradiated for 30 minutes with UVA light to clean and activate the surface. The photocatalysis test involved spray coating the samples with an even layer of the Resazurin based "intelligent ink" (with modifications to the original recipe used by Mills et al.). The intelligent ink consisted of Resazurin (40 mg) redox dye in an aqueous solution (40 mL) with glycerol (3 g) and hydroxyl-ethyl cellulose (0.45 g). The mixture was aged for 24 hours in a fridge (2–5 °C) and thoroughly mixed before use.

UVA light (flux = 4.42×10^{14} photons cm^{-2} s^{-1}) was used to induce the photoreduction of the Resazurin redox dye on the surface of the films and a UV-visible spectrometer was employed to monitor the degradation of the dye. Formal quantum efficiency (FQE) was calculated by dividing the rate of dye molecules destroyed cm^{-2} s^{-1} by the photon flux (4.42×10^{14} photons cm^{-2} s^{-1}). The formal quantum yield (FQY) was calculated by dividing the rate of dye molecules destroyed cm^{-2} s^{-1} by the number of photons absorbed cm^{-2} s^{-1} by the film. The photon flux and photon absorption for each film was determined using a UVX radiometer with a detector for 365 nm radiation attached.

Density functional theory (DFT) calculations were performed using the VASP[45] code, using screened hybrid functional as proposed by Heyd, Scuseria and Ernzerhof (HSE06),[46] employing the same computational set up as used previously to study F-doped anatase TiO_2.[47] The suitability of HSE06 for treating defects in anatase TiO_2 has been rigorously checked, see References.[48–50] In the bulk, we have tested two doping mechanisms; Nb replacing a lattice titanium with the injection of a free electron into the conduction band, (Nb_{Ti} + e) and Nb replacing a lattice titanium, but compensated by the reduction of a neighbouring lattice Ti^{4+} to Ti^{3+}. The formation energy of these defects are calculated using the standard approach,[51,52] using the chemical potential limits calculated previously for anatase TiO_2.[47]

To gain information of surface segregation, and compensation effects, we have also calculated the formation energy of both Nb-doping compensation mechanisms on the (101) surface of anatase TiO_2. The surface was cleaved using the Metadise code,[53] yielding a 72 atom surface, 20.04 Å thick with a vacuum thickness of 22.24 Å. Dopants on the surface were tested on a

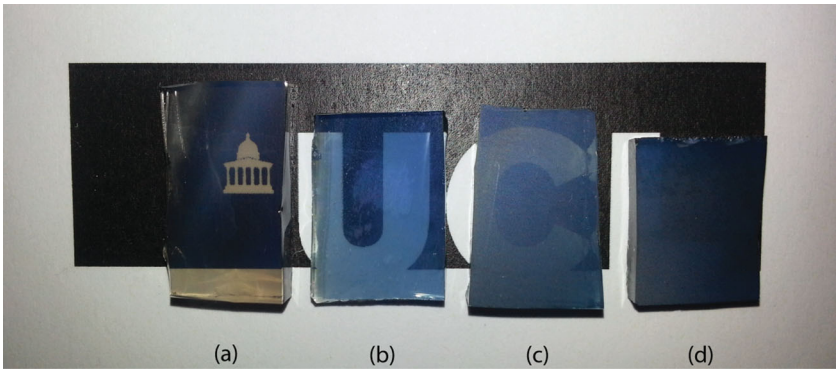

Figure 1. Photograph of a) pristine TiO_2 film, b) $Ti_{0.96}Nb_{0.04}O_2$ film (5 mol.% Nb/Ti in solution), c) $Ti_{0.93}Nb_{0.07}O_2$ film (10 mol.% Nb/Ti in solution), and d) $Ti_{0.86}Nb_{0.14}O_2$ (20 mol.% Nb/Ti in solution) film. Note the intensity of the blue colour increases with Nb content in the films.

$2 \times 1 \times 1$ 144 atom surface. Doping was considered on both sides of the slab, to avoid dipole errors, and all atoms were allowed to relax, using a consistent set up to the bulk calculations.

3. Results and Discussion

Optically transparent and electrically conductive niobium doped titanium dioxide films were deposited on silica coated float glass by the AACVD reaction of $Ti(OEt)_4$ and $Nb(OEt)_5$ in toluene. The undoped TiO_2 films were transparent but upon doping with Nb they became increasingly blue in colour (**Figure 1**).

The AACVD reaction for each system was carried out at 500 °C. The films deposited were uniform, showed excellent coverage across the glass substrates and were adherent, passing the Scotch tape test.

The X-ray diffraction patterns of the as-deposited films formed by AACVD (**Figure 2**) confirmed the presence of anatase TiO_2. Anatase TiO_2 crystallizes in the $I4_1/amdz$ space group and the lattice parameters of the body centred unit cell are a = 3.782 Å, c = 9.504 Å. Only reflections associated with the anatase form of TiO_2 were observed by PXRD. The slight broad feature at around 20° 2θ is due to amorphous scattering of the X-rays by the underlying glass substrate. Notable shifts in the PXRD patterns towards lower 2θ, compared to undoped anatase TiO_2, were observed with increasing Nb content in the starting solution, this was understandable as the ionic radius of Nb^{5+} is larger than of Ti^{4+} ca. 0.03 Å.

To confirm this, Le Bail models were fitted to the data using the GSAS and EXPGUI suite, to obtain the unit cell parameters and determine the expansion in the unit volume, if any. It was assumed that the zero offset did not change from one run to the next and a value of 2.2° was chosen and applied to all the data before the least squares analysis, in which the zero offsets were not refined but the sample displacement parameter was.[30,54]

The lattice constants a and c increased proportionally with niobium content in the films as determined by WDX analysis as shown in **Table 1**. WDX analysis revealed that the incorporation of Nb into anatase TiO_2 was essentially linear, following the increments of niobium in the starting solution but the doping efficiency was around 25%. The original paper on Nb:TiO_2 by Furubayashi et al. noted an increase in a and c parameters from pristine TiO_2. Experimental studies by Kurita et al. saw expansion in the c parameter but no change in the a parameter.[55] Sheppard et al. however noted the opposite.[54] Computational studies by Orita observed that for 2 at.% Nb:TiO_2 the unit cell parameters were a = 3.876 Å and c = 9.758 Å consistent with the results in this paper, however there appears to be no general consensus on the change in the crystal structure upon doping TiO_2 with niobium.[35]

The unit cell volume also increased proportionally with Nb content in solution and in the films, as shown in Table 1. The PXRD data also revealed that the intensity of the reflections for undoped TiO_2 follow that of the bulk powder, but upon doping with niobium strong preferred orientation of the (211) reflection is observed. This was also observed by Kafizas et al. who synthesized Nb:TiO_2 films by combinatorial atmospheric pressure CVD. This is in contrast to PVD methods where preferred orientation is observed in the (200) plane.[21]

The film microstructure and thickness was investigated with scanning electron microscopy (SEM). The as-deposited films were composed of granular pyramidal-like features as can

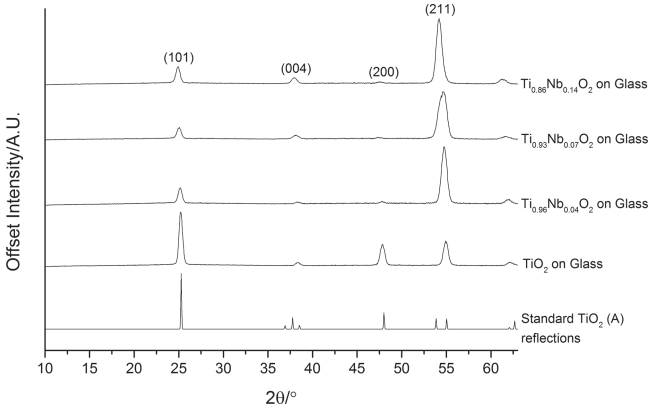

Figure 2. X-ray diffraction pattern of simulated anatase TiO_2, TiO_2 on glass and doped Nb:TiO_2 films on glass from starting solutions of 5 mol.%, 10 mol.% and 20 mol.% Nb/Ti in solution. Note the shift of TiO_2 reflections to lower 2θ with increasing niobium concentration in the films.

Table 1. Nb:Ti at.% as determined by WDX analysis and the corresponding lattice parameters a and c with increasing Nb content. Lattice parameters obtained from Le Bail fitting of models to the data. The associated fitted R_{wp} for the goodness of fit is given also, below 10% indicates a good fit.

Nb content in solution [mol.%]	Nb:Ti by WDX [at.%]	a [Å]	c [Å]	Unit Cell Volume [Å^3]	Fitted R_{wp} [%]
0	0	3.8058(1)	9.5923(19)	138.936(24)	7
5	1.22:33.07	3.8064(1)	9.6613(25)	139.975(34)	7
10	2.53:31.97	3.8183(1)	9.7203(41)	141.718(55)	9
20	4.98:29.52	3.8408(2)	9.7605(24)	143.986(43)	8

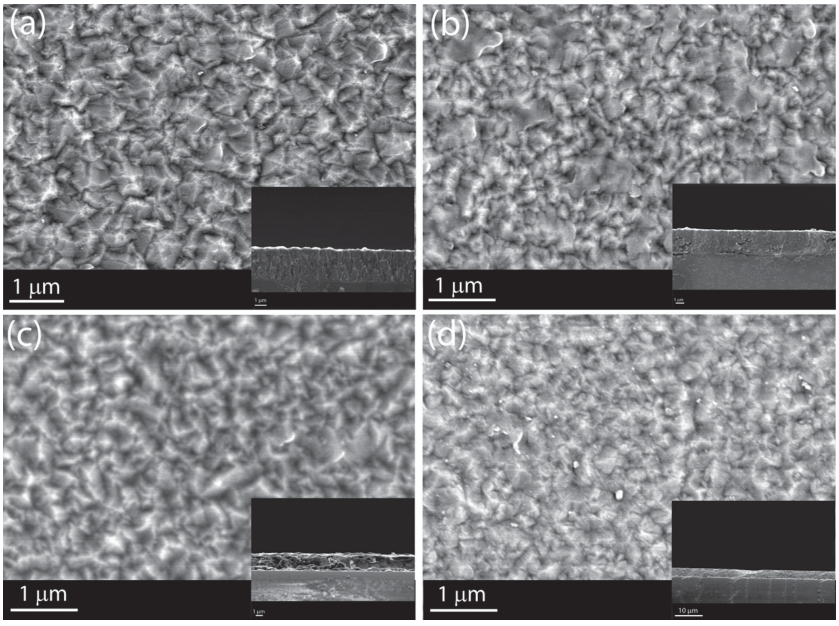

Figure 3. a) Top down SEM image of undoped anatase TiO_2 film on glass (inset shows side-on image), b) top down SEM image of $Ti_{0.96}Nb_{0.04}O_2$ (5 mol.% Nb/Ti in solution) film on glass (inset shows side-on image), c) top down SEM image of $Ti_{0.93}Nb_{0.07}O_2$ (10 mol.% Nb/Ti in solution) film on glass (inset shows side-on image), d) top down SEM image of $Ti_{0.86}Nb_{0.14}O_2$ (20 mol.% Nb/Ti in solution) film on glass (inset shows side-on image).

be seen from **Figure 3**. The microstructure did not appear to change with the introduction of niobium into the system and the thickness of the films was fairly consistent throughout, between 2–2.5 μm. From PXRD, however, it was noted that preferred orientation of the crystallites became apparent with the introduction of niobium into the system from a random orientation of crystallites to the (211) orientation dominating the PXRD pattern.

Hall effect measurements were conducted on the doped titanium dioxide films formed in this work by using the van der Pauw technique to determine the electrical properties of the films. The Hall effect measurements indicated that the films displayed *n*-type conductivity indicating electrons as the dominant charge carrier species. Plain TiO_2 films displayed too high a resistivity for Hall effect studies but crude analysis using a two-point probe indicated a resistance in the MΩ region. Doping with as little as 1 at.% niobium into the TiO_2 structure resulted in a dramatic decrease in the sheet resistance by four orders of magnitude to 260 Ω sq^{-1} with a specific resistivity of 5.8×10^{-2} Ω cm and a charge carrier concentration of the order of 10^{18} cm^{-3}. The mobility of the charge carriers was 11.6 cm^2 V^{-1} s^{-1}. The increased conductivity can be explained by the delocalization of electrons, by niobium doping, into the conduction band of the titanium dioxide. Further doping with niobium to 2.5 at.% results in a further decrease in the sheet resistance to 13 Ω sq^{-1}.

This decrease in sheet resistance was attributed to an increase in charge carrier concentration by two orders of magnitude but there was a decrease in the mobility of the charge carriers to 5 cm^2 V^{-1} s^{-1}. The sheet resistance minimized to 6 Ω sq^{-1} for ≈5 at.% Nb:TiO_2 films and the charge carrier concentration further increased to 2×10^{21} cm^{-3} but the mobility of the charge carriers also minimized to 2 cm^2 V^{-1} s^{-1} as shown in **Table 2**. Gordon et al.[39] synthesized Nb:TiO_2 films with sheet resistances of 25 Ω sq^{-1} for 2 μm thick films with 10 at.% Nb doping. The sheet resistance reported for our films, with 5 at.% Nb, is 4 times less than that reported by Gordon et al. with a similar thickness with comparable charge carrier concentrations but increased charge carrier mobility 2.0 cm^2 V^{-1} s^{-1} compared to 0.7 cm^2 V^{-1} s^{-1} by Gordon et al.[39]

An indication of doping can be gleaned from the Hall effect measurements but in order to substantiate transport measurements, the oxidation state of the metal atoms must be determined to gauge the success of doping donor atoms into the host framework. X-ray photoelectron spectroscopy (XPS) was used to observe transitions from titanium/niobium orbitals into the continuum and thus determine the oxidation state of titanium/niobium species. Niobium doping results in electrons charge compensating the overall positive charge of the TiO_2 framework as a result of Nb^{5+} substituting Ti^{4+} sites in the lattice and the electrons can form reduced Ti or Nb. **Figure 4** shows the XPS spectra for pristine TiO_2 and Nb:TiO_2 films. Pristine TiO_2 (Figure 4a) films deposited on glass only showed Ti^{4+} states with a binding energy (BE) of 458.5 eV for the Ti $2p_{3/2}$ transition.[14] Upon doping with Nb, $Ti_{0.96}Nb_{0.04}O_2$ (Figure 4b) films showed predominantly Ti^{4+} with a BE of 458.3 eV for the Ti $2p_{3/2}$ transition although there was some asymmetry to the Ti $2p_{3/2}$ peak, that could be fitted/modelled with Ti^{3+} states. Nb was also detected by XPS for the $Ti_{0.96}Nb_{0.04}O_2$ sample. Figure 4c shows the XPS spectra for $Ti_{0.93}Nb_{0.07}O_2$ films and it can clearly be seen that there are well-defined Ti^{3+} states as well as Ti^{4+}

Table 2. Electrical properties of as deposited undoped TiO_2 and Nb:TiO_2 films.

Nb:Ti in solution [mol.%]	Nb:Ti in film [at.%]	Film Thickness [μm]	Sheet resistance [Ω sq^{-1}]	ρ [Ω cm]	μ [cm^2 V^{-1} s^{-1}]	N [cm^{-3}]
0	0	2.6	–	–	–	–
5	1.22:33.07	2.4	260	5.8×10^{-2}	11.6	9.3×10^{18}
10	2.53:31.97	1.9	13	2.4×10^{-3}	4.9	5.2×10^{20}
20	4.98:29.52	2.1	6	1.3×10^{-3}	2.0	2.4×10^{21}

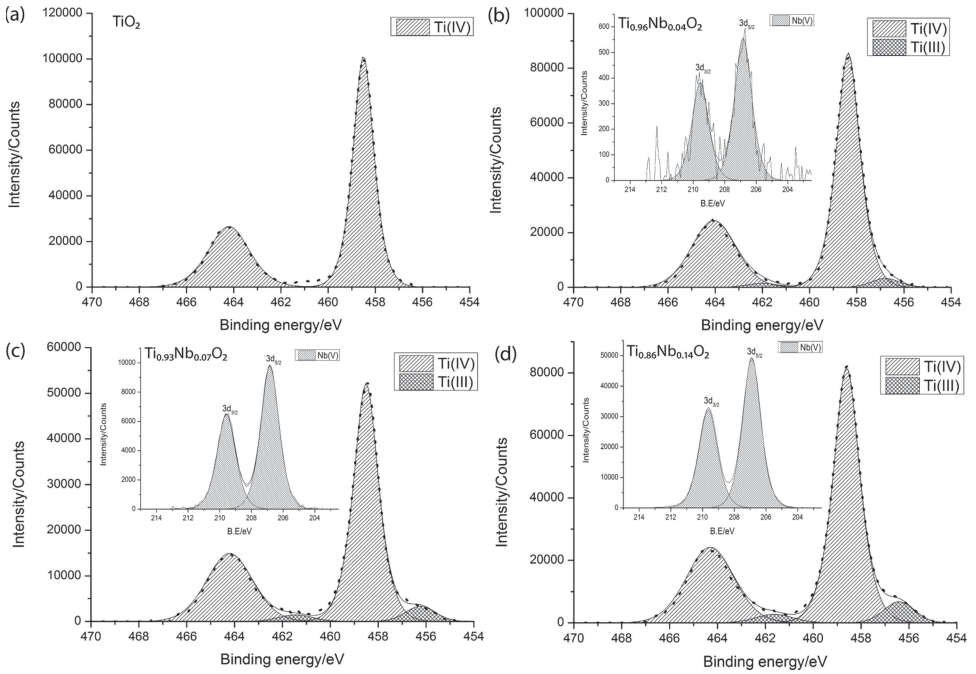

Figure 4. XPS spectra of a) pristine TiO_2 film showing Ti^{4+} state only with a BE of 458.5 eV for the $2p_{3/2}$ transition, b) $Ti_{0.96}Nb_{0.04}O_2$ film showing predominantly Ti^{4+} states with a BE of 458.3 eV for the $2p_{3/2}$ transition and some Ti^{3+} corresponding to a BE of 456.6 with inset showing the Nb^{5+} state with a BE of 206.8 eV for the $3d_{5/2}$ transition, c) $Ti_{0.93}Nb_{0.07}O_2$ film showing Ti^{4+} state with a BE of 458.6 eV for the $2p_{3/2}$ transition and Ti^{3+} state with a BE of 456.1 eV for the $2p_{3/2}$ transition with inset showing Nb^{5+} state with a BE of 206.8 eV for the $3d_{5/2}$ transition, and d) $Ti_{0.86}Nb_{0.14}O_2$ film showing Ti^{4+} state with a BE of 458.6 eV for the $2p_{3/2}$ transition and Ti^{3+} states with a BE of 456.3 eV for the $2p_{3/2}$ transition with inset showing Nb^{5+} state with a BE of 206.9 eV for the $3d_{5/2}$ transition. The dots are experimental data points and the solid lines are best fits to the data. The data was treated with a Shirley background and individual Gaussian/Lorentzian functions for Nb(V), Ti(IV) and Ti(III) final states.

states. The BE of the Ti^{3+} states corresponds to 456.1 eV for the $2p_{3/2}$ transition with the inset showing Nb^{5+} state with a BE of 206.8 eV for the $3d_{5/2}$ transition. The Nb $3d_{5/2}$ transition is of higher intensity compared to films with 1 at.% Nb clearly showing increased Nb content in the films with increasing Nb content in the starting solution. Films with ≈5 at.% Nb ($Ti_{0.86}Nb_{0.14}O_2$) again showed Ti^{3+}/Ti^{4+} states with a higher concentration of reduced Ti states corresponding to the higher Nb concentration in the films also.

These reduced titanium states were observed by Liu et al.[31] using XPS. From this, they concluded that electrons and not point defects were the compensating mechanism as a result of Nb doping. Liu et al. had to anneal their samples in a N_2 environment to improve the room temperature conductivity, even with the presence of Ti^{3+} states to improve the grain size and particle connectivity.[31] It is widely accepted that TCO systems prepared by chemical methods, as opposed to physical methods, often display lower dc conductivity mainly due to grain boundary scattering and a larger number of defects and imperfections in the nanosized crystallites. Using doped titanium dioxide as a potential replacement for conventional TCO materials based on tin/indium is complicated further by the noticeable lattice expansion when Nb is introduced into the crystal structure. This expansion in the crystal structure with increasing dopant concentration decreases the mobility of the charge carriers. For TCO materials based on tin/indium, such a large deformation in the crystal structure is not observed and higher mobilities are often reported for these materials. Nemec et al. used time-domain terahertz transmission spectroscopy and microwave impedance spectroscopy to investigate the dielectric and conduction properties of undoped and niobium doped titanium dioxide mesoporous pellets.[56] From this work they concluded that transport of electrons in the doped samples occurred by a hopping mechanism (low mobility) between the reduced Ti^{3+} states and not by the free electron motion in delocalized conduction band states (high mobility). This can be inferred from the XPS results of our samples, as the number of Ti^{3+} states increases with increasing niobium concentration in the starting solution, the mobility of the charge carriers decreases due to somewhat localized nature of the free electrons.

Nb:TiO_2 is similar to Nb:$SrTiO_3$ (STO) in that the oxidation state of titanium can be regarded as fluctuating between 3+ and 4+ on a time scale longer than the photoemission process (≈10^{-16} s) and the photoemission process gives a snapshot of this 3+/4+ exchange giving rise to a double peaked Ti $2p$ core photoemission spectrum.[33,57,58] As the photoemission initial state of Nb:STO can be described a fraction x of Ti sites with a nominally d^1 configuration and the rest with d^0 configuration so can the Nb:TiO_2 system. This picture can be used to describe excitations near the E_F.

Figure 5 shows the valence band XPS of TiO_2 and $Ti_{0.86}Nb_{0.14}O_2$ thin film samples referenced to the Fermi level E_F. It can seen that Nb doping causes the Fermi edge to lie within the conduction band as well as causing a notable shift of the valence band edge towards higher binding energy

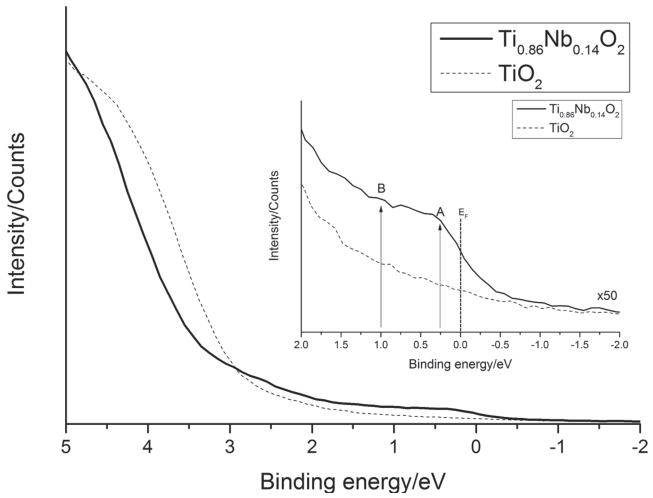

Figure 5. Valence band XPS of TiO_2 film and $Ti_{0.86}Nb_{0.14}O_2$ showing referenced to the Fermi level E_F. It can seem that with Nb doping that the Fermi edge lies within the conduction band and a notable shift of the valence band edge towards higher binding energy indicating Burstein–Moss filling of the conduction band. The inset shows magnified valence band region highlighting two spectral features marked A and B. A and B are due to correlation effects of the conduction electrons resulting in coherent and incoherent screened final states in the photoemission process.

indicating Burstein-Moss filling of the conduction band. The inset shows the magnified valence band region highlighting two spectral features marked **A** and **B**. Feature **A** was assigned to a final coherent (delocalized) state screened by electrons in the conduction band having mainly *d* character.[33,57,58] Feature **B** was due to correlation effects of the conduction electrons due to incoherent (localized) screened final states in the photoemission process. From these considerations, we concluded that peaks A and B originated from a Ti orbital initially having a nominal d^1 configuration. This phenomenon is shown schematically in **Figure 6**.

In order to understand the nature of the excess electron donated to TiO_2 upon Nb doping, we analysed the degree of localization/delocalization of the excess electrons in our hybrid-DFT calculations. Our results reveal that in the bulk, the formation of a localized polaronic Ti^{3+} state is 0.21 eV less stable than that of a fully delocalized electron in the conduction band, **Figure 7**a,b. This indicates that Nb dopants in the bulk of anatase TiO_2 will donate electrons directly to the conduction band. This is consistent with the degenerate conductivity of Nb-doped samples reported here and elsewhere.[32,33,55,57–60] It should be noted that in rutile TiO_2, the localized electron state is more stable than that of the delocalized state, this can be attributed to the lower conduction band of anatase relative to rutile.[22,61]

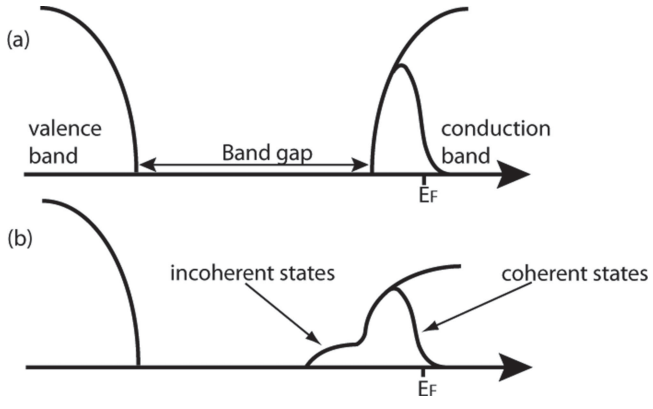

Figure 6. Schematic of the electronic structures near the Fermi level (E_F) within a) band theory and b) when correlation effects are included for the conduction electrons.

On the (101) anatase surface, however, the situation is somewhat different. There are two possible surface dopant positions, five coordinate Ti sites (Ti_{5c}) and six coordinate Ti sites (Ti_{6c}), with Nb preferring the Ti_{6c} site by 0.24 eV. In addition, for both sites, we found that the localized electron polaron was ≈0.03 eV more stable than a delocalized free electron in the conduction band, Figure 7c,d. This energy difference is sufficiently small that at room temperature, you would expect to see a mixture of both Ti^{3+} and free conduction electrons on the surface of anatase. This is consistent with the presence of both localized Ti^{3+} peaks and occupation above the conduction band in the XPS spectra. Under O-rich conditions, the formation energy of an Nb-dopant in the bulk and on the (101) surface is 1.74 eV and 0.20 eV respectively, indicating that under equilibrium conditions, Nb will clearly want to segregate towards the surface.

In order to further confirm the Nb doping in anatase TiO_2 by AACVD grown films, X-ray absorption spectroscopy studies at the Nb and Ti K-edge were performed. Nb K-edge X-ray absorption near edge spectra (XANES) of $Ti_{0.93}Nb_{0.07}O_2$ film is shown in **Figure 8** along with Nb_2O_5.

The Nb-edge features, in particular the shoulder at ca. 18 986 eV indicates that Nb in $Ti_{0.93}Nb_{0.07}O_2$ film is clearly in the 5+ oxidation state as defined by the edge energy with no evidence of Nb^{4+} that would show a shift in the edge energy as well as showing spectral features similar to NbO_2.[62] Some of the spectral features of the $Ti_{0.93}Nb_{0.07}O_2$ film also differ from that of Nb_2O_5 standard indicating that there is no phase segregation in the bulk of the films to NbO_2/Nb_2O_5 and that Nb is substituting on Ti sites in the anatase lattice. Ti K-edge XANES is given in Figure 8b and clearly shows that the $Ti_{0.93}Nb_{0.07}O_2$ film is the anatase phase with no evidence of rutile species or Ti(III) species, further supporting DFT calculations highlighting the stability of Ti(III) at the surface only. Analysis of the Nb K-edge EXAFS data revealed that the average Nb-O distance of the first neighbour is significantly shorter than that observed for Nb_2O_5 and is found to be very similar to that of Ti-O distance in TiO_2 anatase. More importantly, the second and third Nb-Ti distances were found to be similar to that observed for Ti-Ti in TiO_2 anatase phase. The results of the analysis are given in **Table 3** and the best fit between experimental data and the calculated EXAFS along with the associated Fourier transforms are shown in **Figure 9**. These results clearly provide a direct evidence for the substitution of Nb^{5+} ions in the TiO_2 lattice.

The room temperature transmission characteristics of the doped titanium dioxide films deposited by AACVD were investigated using visible/near IR spectrometry. The UV-vis spectrum shown in **Figure 10** was taken using an air background and pristine TiO_2 films were transparent across the visible (≈60% transmission at 700 nm in air, including the substrate

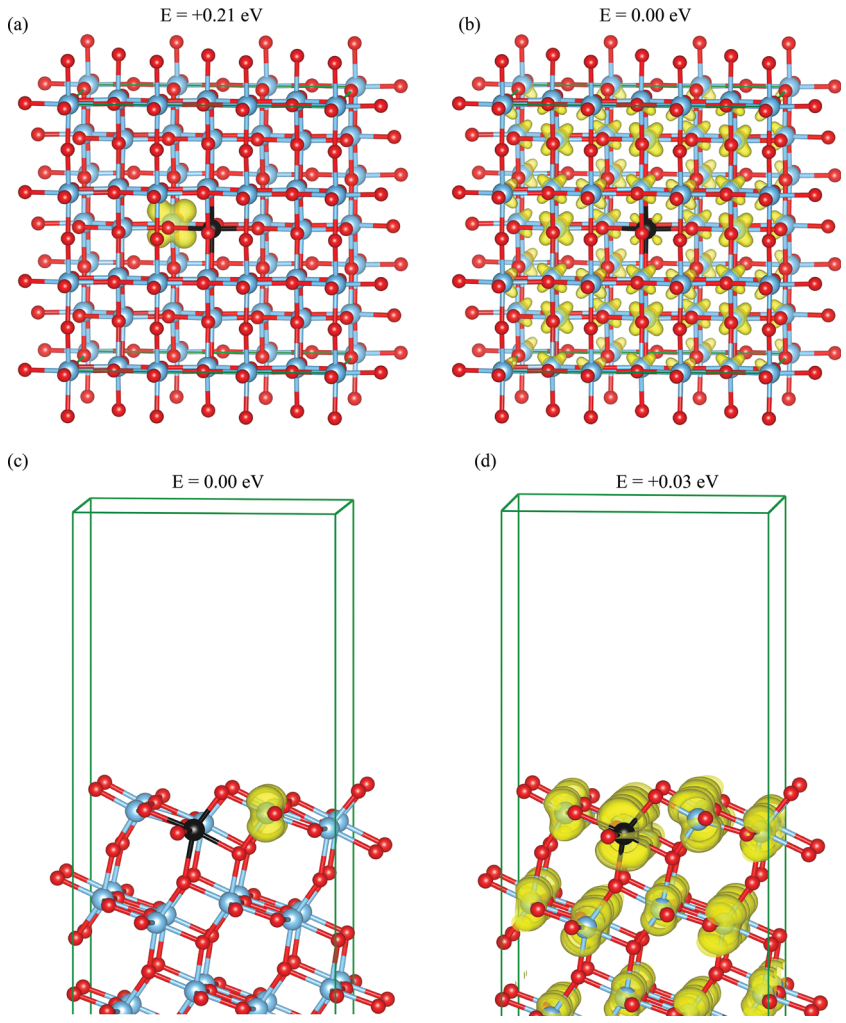

Figure 7. HSE06 calculated charge density plots for Nb doped Anatase TiO_2 bulk with a) a localized electron and b) a delocalized excess electron. The lower panels display the charge density for a Nb-doped anatase (101) surface with c) a localized excess electron and d) a delocalized electron. Blue, black, and red spheres represent titanium, niobium and oxygen ions respectively. The yellow isosurfaces shown is set at 0.05 electrons $Å^{-3}$ for (a) and (c), and 0.005 electrons $Å^{-3}$ for (b) and (d).

absorbance). Figure 10 shows that transmittance decreases for niobium doped titanium dioxide samples compared to pristine TiO_2 around 450–600 nm. This could be due to a *d-d* transition as a result of Ti^{3+} states.[63] This phenomenon was also observed by Mulmi et al. for Nb:TiO_2 single crystals who also attributed the colour to *d-d* transition from Ti^{3+} states.[63]

The indirect direct bandgaps were determined by constructing Tauc plots using the $(\alpha h\nu)^{1/2}$ relation. These ranged from 3.23 eV for TiO_2 to 3.35 eV for films containing 5 at.% Nb. This effective increase can be rationalized by the Burstein–Moss effect, as electrons populate the conduction band, the optical bandgap is effectively increased.[64,65]

The photocatalytic abilities of pristine TiO_2, $Ti_{0.96}Nb_{0.04}O_2$, $Ti_{0.93}Nb_{0.07}O_2$ and $Ti_{0.86}Nb_{0.14}O_2$ films were studied using Resazurin dye based "intelligent ink" and are shown in **Figure 11**. The ink contained Resazurin dye, hydroxy-ethyl cellulose, glycerol and distilled water.[66] Resazurin dye was used to infer the photocatalytic activity of the films as it allows a rapid and simple method to obtain an accurate reaction rate, formal quantum efficiency (FQE) and yield (FQY). Other techniques, such as the stearic acid, methyl orange and methylene blue tests, for monitoring phototcatalytic activity can take up to many days to determine the reaction rate and require expensive equipment.[67–69] The photoreduction of the dye was induced by a UVA light source with a photon flux of 4.42×10^{14} photons cm^{-2} s^{-1} and the degradation of the dye with irradiation time was followed via UV-vis spectroscopy. The formal quantum efficiency (FQE) and formal quantum yield (FQY) were calculated.

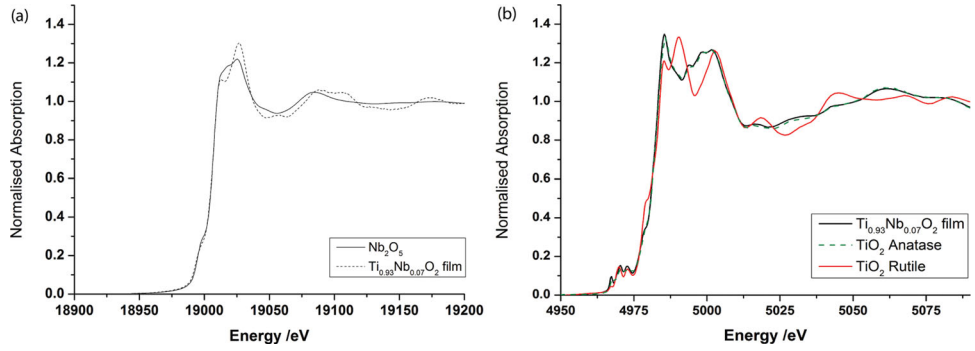

Figure 8. XANES spectra of a) of $Ti_{0.93}Nb_{0.07}O_2$ film and Nb_2O_5 powder at the Nb K-edge. The XANES spectra clearly show that Nb in $Ti_{0.93}Nb_{0.07}O_2$ film is in the 5+ oxidation state with no evidence of NbO_2 in the bulk as defined by the position of the edge energy. The spectral features of Nb in the $Ti_{0.93}Nb_{0.07}O_2$ film also differ from that of Nb_2O_5 indicating that there is no phase segregation in the bulk of the films to Nb_2O_5 and that Nb is substituting on Ti sites in the anatase lattice and b) of $Ti_{0.93}Nb_{0.07}O_2$ film, TiO_2 anatase powder and TiO_2 rutile powder at the Ti K-edge. Note the XANES spectra at the Ti K-edge clearly shows the $Ti_{0.93}Nb_{0.07}O_2$ film as adopting the anatase polymorph of TiO_2 with no evidence of rutile formation or Ti(III) states in the bulk as also seen by DFT calculations.

Table 3. Structural Parameters Obtained from the Analysis of Nb K-edge EXAFS data on $Ti_{0.93}Nb_{0.07}O_2$ film.

System	Edge	Atom Pair	N	R [Å]	σ^2 [Å^2]	Fit Index
TiO_2	Ti	Ti-O	6	–	–	–
		Ti-Ti	4	–	–	–
		Ti-Ti	4	–	–	–
$Ti_{0.93}Nb_{0.07}O_2$ Film	Nb	Nb-O	6	1.99	0.003	38.95
		Nb-Ti	4	3.11	0.003	
		Nb-Ti	4	3.92	0.005	

The pristine TiO_2 sample was able to reduce the Resazurin dye at a rate of 5.3×10^{11} dye molecules s^{-1} cm^{-2}, superior to the $Ti_{0.96}Nb_{0.04}O_2$, which was able to degrade the dye at a rate of 4.3×10^{11} dye molecules s^{-1} cm^{-2}. The $Ti_{0.93}Nb_{0.07}O_2$ film in comparison degraded the dye at a higher rate of with 7.8×10^{11} dye molecules s^{-1} cm^{-2}. Suggesting that an increase in the Nb concentration in the films gave an increase in the rate of dye degradation as expected. However, for $Ti_{0.86}Nb_{0.14}O_2$ film, the rate of dye degradation was an order of magnitude smaller than the other doped samples as well as the pristine TiO_2. These rates are an order of magnitude lower than the rate of Resazurin degradation found for a combinatorial APCVD Nb doped TiO_2 film studied by Kafizas et al.[21] They found for a region doped with 0.09 at.% Nb the rate of dye degradation was 3.4×10^{12} dye molecules s^{-1} cm^{-2}.

Taking the rates of degradation into consideration with the UVA photon flux and UVA photon absorption for each film enabled the calculation of the formal quantum efficiency (FQE) (the number of dye molecules destroyed per incident photon) and the formal quantum yield (FQY) (the number of dye molecules destroyed per absorbed photon) respectively. $Ti_{0.93}Nb_{0.07}O_2$ sample showed the best FQE and FQY results of all the films tested with 1.76×10^{-3} dye molecules/incident photon and 1.97×10^{-3} dye molecules/absorbed photon respectively.

The $Ti_{0.96}Nb_{0.04}O_2$ sample showed a FQE of 1.0×10^{-3} dye molecules/incident photon and FQY of 1.60×10^{-3} dye molecules/absorbed photon. The photocatalytic activity of the $Ti_{0.86}Nb_{0.14}O_2$ sample was inferior compared to the Pristine TiO_2, $Ti_{0.96}Nb_{0.04}O_2$ and $Ti_{0.93}Nb_{0.07}O_2$ samples with both the FQE and the FQY an order of magnitude lower at 1.56×10^{-4} dye molecules/incident photon and 1.87×10^{-4} dye molecules/absorbed photon respectively. Comparisons of these results with the industry standard Pilkington Activ, a commercially available self-cleaning glass coated with 15 nm of anatase TiO_2 grown by atmospheric pressure CVD (APCVD) between 620–650 °C, suggested that the pristine TiO_2, $Ti_{0.96}Nb_{0.04}O_2$ and $Ti_{0.93}Nb_{0.07}O_2$ had much better FQEs than Activ. This was primarily due to the more structured morphology of the AACVD grown samples and the higher thickness compared to Activ; Pilkington Acitv has a morphology made up of flat domes of TiO_2.[70,71] As seen from SEM, the pristine TiO_2 and the Nb doped TiO_2 films all had a pyramidal granular morphology with a larger surface area than Activ.

When taking into consideration the changes UV light absorption from film to film, by determining the FQY, the photocatalytic activity of $Ti_{0.93}Nb_{0.07}O_2$ is superior with 1.97×10^{-3} dye molecules/absorbed photon. It also has a FQY 1.25 times better than the pristine TiO_2 sample (1.57×10^{-3} dye molecules/absorbed photon). The FQY of the $Ti_{0.96}Nb_{0.04}O_2$ sample is smaller than that of the pristine TiO_2 sample. As expected the $Ti_{0.86}Nb_{0.14}O_2$ film had a FQY of 1.87×10^{-4} dye molecules/absorbed photon which is an order of magnitude worse than the other samples. This suggests that upon doping the photocatalytic activity increases not only due to an increase in surface structure but also due to the native defects such as oxygen vacancies in TiO_2 being filled by the dopant thus allowing promotion of electrons from the valence band to the conduction band to occur more easily.[69] Increasing the dopant concentration further, such as in the case of $Ti_{0.86}Nb_{0.14}O_2$, results in a decrease in the FQY as the dopants act as recombination sites for electrons and holes.[72]

A recent review by Ginley et al. highlighted the potential of a solution processing route to Nb:TiO_2 films. Current PVD routes to growing highly conductive Nb:TiO_2 films are problematic given the low oxygen partial pressure required for high carrier generation in anatase Nb:TiO_2 which in turn favours growth of rutile TiO_2 phase which is semiconducting. Some methods to overcome this have been to deposit epitaxial films by PLD on lattice matched substrates, which is not a practical solution as these substrates are expensive and not suitable for industrial applications. Other methods to obtain electrically conductive Nb:TiO_2 have been to deposit an anatase seed layer at high oxygen partial pressure followed by post treatment at

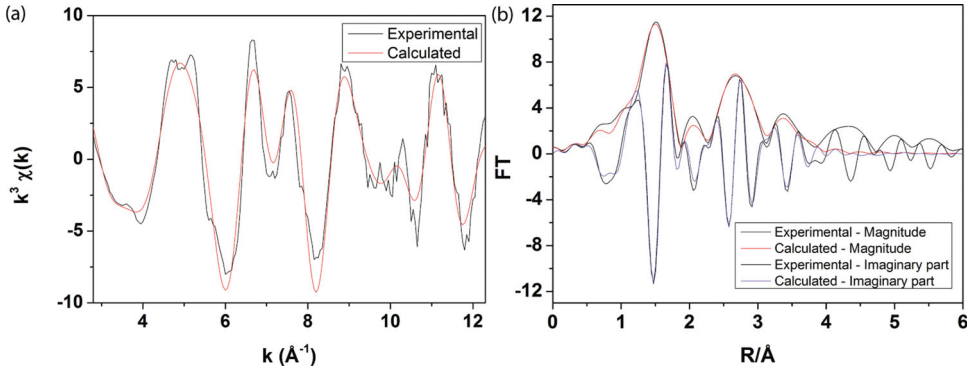

Figure 9. a) Nb K-edge EXAFS for $Ti_{0.93}Nb_{0.07}O_2$ film and b) associated Fourier transforms showing experimental and calculated data for real and imaginary components.

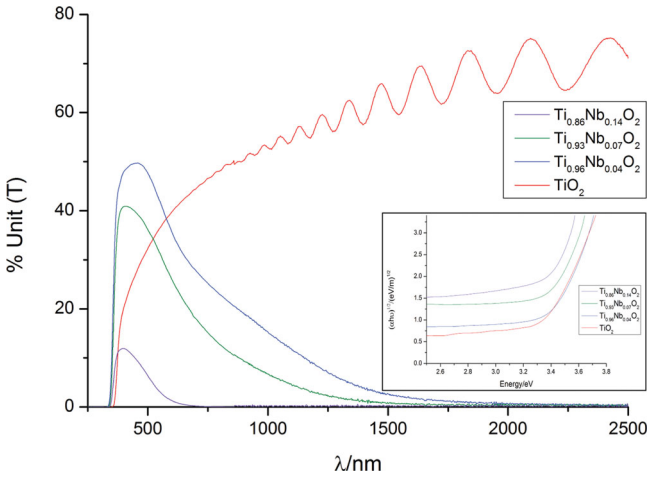

Figure 10. Optical transmission spectrum taken against an air background showing undoped anatase TiO_2 films and Nb:TiO_2 films grown (0, 5, 10 and 20 mol.% Nb/Ti solutions) at 500 °C on glass by AACVD reaction of $Ti(OEt)_4$ and $Nb(OEt)_5$.

low oxygen partial pressure. Another method has been to deposit an amorphous TiO_2 layer by PVD with a post-deposition H_2 annealing step to obtain Nb:TiO_2 films with adequate properties.[73]

We have demonstrated that transparent and electrically conductive Nb:TiO_2 films can be deposited on inexpensive glass substrates in one-step, without post-deposition annealing and expensive vacuum systems using AACVD. AACVD is potentially scalable and we have shown that the electronic, crystal and surface texture properties of niobium doped titanium dioxide films can be tailored to a specific application.

Thus, Nb:TiO_2 synthesized by AACVD combine four functional properties (photocatalysis, electrical conductivity, optical transparency and blue colouration) within the same layer, making it a promising alternative to conventional TCO materials.

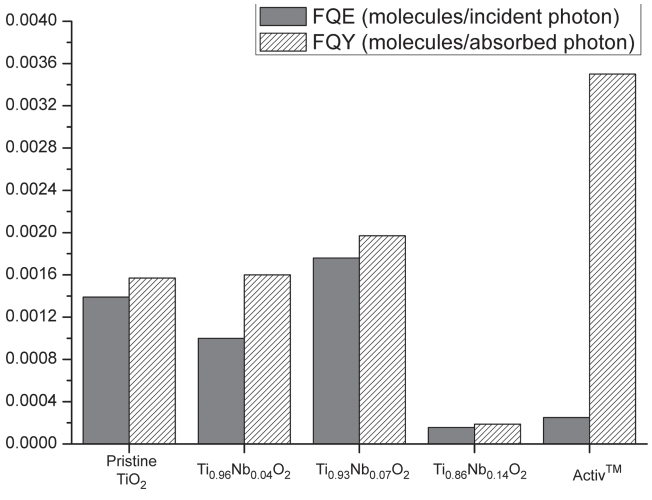

Figure 11. Graph comparing the formal quantum efficiency and yield of the photodegradation of Resazurin redox dye on $Ti_{0.96}Nb_{0.04}O_2$, $Ti_{0.93}Nb_{0.07}O_2$ and $Ti_{0.86}Nb_{0.14}O_2$.

4. Conclusions

AACVD was shown to be an effective and simple method for the deposition of transparent and conductive niobium doped titanium dioxide films. Doping Nb into the Ti sites resulted in *n*-type conductivity as determined by Hall effect measurements. The doped films displayed significantly improved electrical properties compared to pristine TiO_2 films. For $Ti_{0.86}Nb_{0.14}O_2$ the charge carrier concentration was 2×10^{21} cm^{-3} with a mobility of 2 cm^2 V^{-1} s^{-1}. The corresponding sheet resistance was as low as 6.5 Ω sq^{-1} making the films suitable candidates for transparent conducting oxide (TCO) materials. These films could be used as electrodes in photovoltaics or in architectural glazing. The surface morphology together with the opto-electronic properties makes this material ideal for PV applications requiring light trapping and scattering. Control over the carrier mobility, charge-carrier density, crystallinity and the surface morphology of the films have been shown to be highly dependent upon the dopant introduction using this technique. This work demonstrates that compared to PVD and APCVD, AACVD is vital to synthesising Nb:TiO_2 films in one step for TCO and photocatalytic applications. In addition, our results provide a blueprint for the potential move away from conventional TCO materials based on tin and indium, towards titanium based TCO materials. Crucially, the method can be used for tailoring functional properties of the films to specific applications, including transparent conducting materials for photovoltaic devices as well as photocatalytic materials.

Acknowledgements

D.S.B. would like to thank Prof. Russell Egdell for useful discussions. G.S. would like to thank Diamond Light source for providing beam time and facility under the grant reference SP8071–6.

Received: February 4, 2014
Revised: March 27, 2014
Published online: May 26, 2014

[1] P. P. Edwards, A. Porch, M. O. Jones, D. V. Morgan, R. M. Perks, *Dalton Trans.* **2004**, 2995.
[2] D. Belanger, J. P. Dodelet, B. A. Lombos, J. I. Dickson, *J. Electrochem. Society* **1985**, *132*, 1398.
[3] P. Ãgoston, K. Albe, R. M. Nieminen, M. J. Puska, *Phys. Rev. Lett.* **2009**, *103*.
[4] T. Minami, *MRS Bulletin* **2011**, *25*, 38.
[5] D. S. Bhachu, M. R. Waugh, K. Zeissler, W. R. Branford, I. P. Parkin, *Chem. Eur. J.* **2011**, *17*, 11613.
[6] B. O'Regan, M. Grätzel, *Nature* **1991**, *353*, 737.
[7] C. Uhrich, R. Schueppel, A. Petrich, M. Pfeiffer, K. Leo, E. Brier, P. Kilickiran, P. Baeuerle, *Adv. Funct. Mater.* **2007**, *17*, 2991.
[8] J. Müller, B. Recha, J. Springer, M. Vanecek, *Solar Energy* **2004**, *77*, 910.
[9] C. R. A. Catlow, A. A. Sokol, A. Walsh, *Chem. Commun.* **2011**, *47*, 3386.
[10] D. S. Bhachu, G. Sankar, I. P. Parkin, *Chem. Mater.* **2012**, *24*, 4704.
[11] K. G. Godinho, A. Walsh, G. W. Watson, *J. Phys. Chem. C* **2009**, *113*, 439.

[12] C. E. Knapp, G. Hyett, I. P. Parkin, C. J. Carmalt, *Chem. Mater.* **2011**, *23*, 1719.
[13] C. E. Knapp, A. Kafizas, I. P. Parkin, C. J. Carmalt, *J. Mater. Chem.* **2011**, *21*, 12644.
[14] P. J. Marchand, I. Hassan, I. Parkin, C. J. Carmalt, *Dalton Trans.* **2013**.
[15] R. B. Goldner, H. M. Haskal, *Appl. Opt.* **1975**, *14*, 2328.
[16] J. Hu, R. G. Gordon, *J. Appl. Phys.* **1992**, *71*, 880.
[17] S. K. Ghandhi, R. J. Field, J. R. Shealy, *Appl. Phys. Lett.* **1980**, *37*, 449.
[18] A. Fujishima, K. Honda, *Nature* **1972**, *238*, 37.
[19] G. Hyett, J. A. Darr, A. Mills, I. P. Parkin, *Chem. Vap. Deposition* **2010**, *16*, 301.
[20] I. P. Parkin, *Chem. Vap. Deposition* **2012**, *18*, 87.
[21] A. Kafizas, C. W. Dunnill, I. P. Parkin, *J. Mater. Chem.* **2010**, *20*, 8336.
[22] D. O. Scanlon, C. W. Dunnill, J. Buckeridge, S. A. Shevlin, A. J. Logsdail, S. M. Woodley, C. R. A. Catlow, M. J. Powell, R. G. Palgrave, I. P. Parkin, G. W. Watson, T. W. Keal, P. Sherwood, A. Walsh, A. A. Sokol, *Nat. Mater.* **2013**, *12*, 798.
[23] H. M. Yates, M. G. Nolan, D. W. Sheel, M. E. Pemble, *J. Photochem. Photobiol. A: Chem.* **2006**, *179*, 213.
[24] C. Das, P. Roy, M. Yang, H. Jha, P. Schmuki, *Nanoscale* **2011**, *3*, 3094.
[25] M. R. Waugh, G. Hyett, I. P. Parkin, *Chem. Vap. Deposition* **2008**, *14*, 366.
[26] K. Sayama, H. Sugihara, H. Arakawa, *Chem. Mater.* **1998**, *10*, 3825.
[27] T. Yoshida, K. Terada, D. Schlettwein, T. Oekermann, T. Sugiura, H. Minoura, *Adv. Mater.* **2000**, *12*, 1214.
[28] J. Y. Yang, W. S. Li, H. Li, Y. Sun, R. F. Dou, C. M. Xiong, L. He, J. C. Nie, *Appl. Phys. Lett.* **2009**, *95*, 213105.
[29] L. R. Sheppard, T. Bak, J. Nowotny, *J. Phys. Chem. B* **2006**, *110*, 22447.
[30] L. R. Sheppard, *J. Phys. Chem. C* **2013**, *117*, 3407.
[31] Y. Liu, J. M. Szeifert, J. M. Feckl, B. Mandlmeier, J. Rathousky, O. Hayden, D. Fattakhova-Rohlfing, T. Bein, *ACS Nano* **2010**, *4*, 5373.
[32] T. Hitosugi, H. Kamisaka, K. Yamashita, H. Nogawa, Y. Furubayashi, S. Nakao, N. Yamada, A. Chikamatsu, H. Kumigashira, M. Oshima, Y. Hirose, T. Shimada, T. Hasegawa, *Appl. Phys. Exp.* **2008**, *1*, 111203.
[33] D. Morris, Y. Dou, J. Rebane, C. E. J. Mitchell, R. G. Egdell, D. S. L. Law, A. Vittadini, M. Casarin, *Phys. Rev. B* **2000**, *61*, 13445.
[34] A. Ghicov, M. Yamamoto, P. Schmuki, *Angew. Chem. Int. Ed.* **2008**, *47*, 7934.
[35] N. Orita, *Jpn. J. Appl. Phys.* **2010**, *49*, 055801.
[36] S. X. Zhang, D. C. Kundaliya, W. Yu, S. Dhar, S. Y. Young, L. G. Salamanca-Riba, S. B. Ogale, R. D. Vispute, T. Venkatesan, *J. Appl. Phys.* **2007**, *102*, 013701.
[37] K. L. Choy, *Prog. Mater. Sci.* **2003**, *48*, 57.
[38] C. Edusi, G. Sankar, I. P. Parkin, *Chem. Vap. Deposition* **2012**, *18*, 126.
[39] S. Hegedus, H. Liang, R. G. Gordon, *AIP Conf. Proc.* **1996**, *355*, 465.
[40] S. O'Brien, M. G. Nolan, M. Çopuroglu, J. A. Hamilton, I. Povey, L. Pereira, R. Martins, E. Fortunato, M. Pemble, *Thin Solid Films* **2010**, *518*, 4515.
[41] A. C. Larson, R. B. Von Dreele, *General Structure Analysis System (GSAS); Los Alamos National Laboratory Report LAUR* **2000**, pp. 86.
[42] B. H. Toby, *J. Appl. Cryst.* **2001**, *34*, 210.
[43] B. Ravel, M. Newville, *J. Synchrotron Radiat.* **2005**, *12*, 537.
[44] S. J. Gurman, N. Binsted, I. Ross, *J. Phys. C: Solid State Physics* **1986**, *19*, 1845.
[45] G. Kresse, J. Hafner, *Phys. Rev. B* **1994**, *49*, 14251.
[46] A. V. Krukau, O. A. Vydrov, A. F. Izmaylov, G. E. Scuseria, *J. Chem. Phys.* **2006**, *125*, 224106.
[47] A. Kafizas, N. Noor, P. Carmichael, D. O. Scanlon, C. J. Carmalt, I. P. Parkin, *Adv. Funct. Mater.* **2013**, DOI:10.1002/adfm.201301333.
[48] V. Çelik, E. Mete, *Phys. Rev. B* **2012**, *86*.
[49] P. Deák, B. Aradi, T. Frauenheim, *Phy. Rev. B* **2011**, *83*.
[50] H. A. Huy, B. Aradi, T. Frauenheim, P. Deák, *Phys. Rev. B* **2011**, *83*.
[51] M. Burbano, D. O. Scanlon, G. W. Watson, *J. Am. Chem. Soc.* **2011**, *133*, 15065.
[52] D. O. Scanlon, P. D. C. King, R. P. Singh, A. de la Torre, S. M. Walker, G. Balakrishnan, F. Baumberger, C. R. A. Catlow, *Adv. Mater.* **2012**, *24*, 2154.
[53] G. W. Watson, E. T. Kelsey, N. H. de Leeuw, D. J. Harris, S. C. Parker, *J. Chem. Soc. Faraday Trans.* **1996**, *92*, 433.
[54] L. R. Sheppard, A. J. Atanacio, T. Bak, J. Nowotny, M. K. Nowotny, K. E. Prince, *J. Solid State Electrochem.* **2008**, *13*, 1115.
[55] D. Kurita, S. Ohta, K. Sugiura, H. Ohta, K. Koumoto, *J. Appl. Phys.* **2006**, *100*, 096105.
[56] H. Němec, Z. Mics, M. Kempa, P. Kužel, O. Hayden, Y. Liu, T. Bein, D. Fattakhova-Rohlfing, *J. Phys. Chem. C* **2011**, *115*, 6968.
[57] Y. Ishida, R. Eguchi, M. Matsunami, K. Horiba, M. Taguchi, A. Chainani, Y. Senba, H. Ohashi, H. Ohta, S. Shin, *Phys. Rev. Lett.* **2008**, *100*.
[58] H. Nogawa, A. Chikamatsu, Y. Hirose, S. Nakao, H. Kumigashira, M. Oshima, T. Hasegawa, *J. Phys. D: Appl. Phys.* **2011**, *44*, 365404.
[59] M. A. Gillispie, M. F. A. M. van Hest, M. S. Dabney, J. D. Perkins, D. S. Ginley, *J. Mater. Res.* **2011**, *22*, 2832.
[60] Y. Furubayashi, T. Hitosugi, Y. Yamamoto, K. Inaba, G. Kinoda, Y. Hirose, T. Shimada, T. Hasegawa, *Appl. Phys. Lett.* **2005**, *86*, 252101.
[61] V. Pfeifer, P. Erhart, S. Li, K. Rachut, J. Morasch, J. Brötz, P. Reckers, T. Mayer, S. Rühle, A. Zaban, I. Mora Seró, J. Bisquert, W. Jaegermann, A. Klein, *J. Phys. Chem. Lett.* **2013**, *4*, 4182.
[62] S. Yoshida, T. Tanaka, T. Hanada, T. Hiraiwa, H. Kanai, T. Funabiki, *Catal. Lett.* **1992**, *12*, 277.
[63] D. D. Mulmi, T. Sekiya, N. Kamiya, S. Kurita, Y. Murakami, T. Kodaira, *J. Phys. Chem. Solids* **2004**, *65*, 1181.
[64] E. Burstein, *Phys. Rev.* **1954**, *93*, 632.
[65] T. S. Moss, *Proc. Phys. Soc. B* **1954**, *67*, 775.
[66] A. Mills, J. Wang, M. McGrady, *J. Phys. Chem. B* **2006**, *110*, 18324.
[67] A. Mills, J. Wang, S.-K. Lee, M. Simonsen, *Chem. Commun.* **2005**, 2721.
[68] A. Mills, *Appl. Catal. B: Environ.* **2012**, *128*, 144.
[69] S. Na-Phattalung, M. Smith, K. Kim, M.-H. Du, S.-H. Wei, S. Zhang, S. Limpijumnong, *Phys. Rev. B* **2006**, *73*.
[70] A. Mills, A. Lepre, N. Elliott, S. Bhopal, I. P. Parkin, S. A. O'Neill, *J. Photochem. Photobiol. A: Chem.* **2003**, *160*, 213.
[71] A. Kafizas, I. P. Parkin, *Chem. Soc. Rev.* **2012**, *41*, 738.
[72] W. Choi, A. Termin, M. R. Hoffmann, *J. Phys. Chem.* **1994**, *98*, 13669.
[73] R. M. Pasquarelli, D. S. Ginley, R. O'Hayre, *Chem. Soc. Rev.* **2011**, *40*, 5406.